Inward and outward migration of massive planets: moving towards a stalling radius

Chiara E. Scardoni, Cathie J. Clarke, Giovanni P. Rosotti, Richard A. Booth, Richard D. Alexander, Enrico Ragusa

Monthly Notices of the ROYAL ASTRONOMICAL SOCIETY

MNRAS **514,** 5478–5492 (2022) https://doi.org/10.1093/mnras/stac1700
Advance Access publication 2022 June 21

Inward and outward migration of massive planets: moving towards a stalling radius

Chiara E. Scardoni,[1]★ Cathie J. Clarke,[1] Giovanni P. Rosotti,[2,3] Richard A. Booth,[4] Richard D. Alexander[2] and Enrico Ragusa[2,5]

[1]*Institute of Astronomy, University of Cambridge, Madingley Road, Cambridge CB3 0HA, UK*
[2]*School of Physics and Astronomy, University of Leicester, University Road, Leicester LE1 7RH, UK*
[3]*Leiden Observatory, Leiden University, PO Box 9513, NL-2300 RA Leiden, the Netherlands*
[4]*Astrophysics Group, Imperial College London, Blackett Laboratory, Prince Consort Road, London SW7 2AZ, UK*
[5]*Univ Lyon, Univ Lyon1, Ens de Lyon, CNRS, Centre de Recherche Astrophysique de Lyon UMR5574, F-69230 Saint-Genis-Laval, France*

Accepted 2022 June 14. Received 2022 June 13; in original form 2022 April 19

ABSTRACT

Recent studies on the planet-dominated regime of Type II migration showed that, contrary to the conventional wisdom, massive planets can migrate outwards. Using 'fixed-planet' simulations, these studies found a correlation between the sign of the torques acting on the planet and the parameter K' (which describes the depth of the gap carved by the planet in the disc). We perform 'live-planet' simulations exploring a range of K' and disc mass values to test and extend these results. The excitation of planet eccentricity in live-planet simulations breaks the direct dependence of migration rate (rate of change of semimajor axis) on the torques imposed, an effect that 'fixed-planet' simulations cannot treat. By disentangling the contribution to the torque due to the semimajor axis evolution from that due to the eccentricity evolution, we recover the relation between the magnitude and sign of migration and K' and argue that this relation may be better expressed in terms of the related gap depth parameter K. We present a toy model in which the sign of planetary migration changes at a limiting value of K, through which we explore planets' migration in viscously evolving discs. The existence of the torque reversal shapes the planetary system's architecture by accumulating planets either at the stalling radius or in a band around it (defined by the interplay between the planet migration and the disc evolution). In either case, planets pile up in the area 1–10 au, disfavouring hot Jupiter formation through Type II migration in the planet-dominated regime.

Key words: accretion, accretion discs – hydrodynamics – planet–disc interactions – protoplanetary discs.

1 INTRODUCTION

Planets form from protoplanetary disc material and continue to interact with this material by exchanging orbital energy and angular momentum via tidal torques. This interaction shapes both planetary orbital architecture and disc structure. Planet–disc interactions have been studied over many decades, long before the detection of the first exoplanet by Mayor & Queloz (1995): see for example Lin & Papaloizou (1979) and Goldreich & Tremaine (1979, 1980). Recent reviews of the topic include Papaloizou & Terquem (2006), Kley & Nelson (2012), Baruteau et al. (2014), Papaloizou (2021), Paardekooper et al. (2022).

Once a planet has formed in a protoplanetary disc, depending on its mass it might be able to open a gap in the disc surface density, or it may remain embedded in the disc. On this basis, planet migration can be classified (e.g. Artymowicz 1993; Ward 1998; Kley & Nelson 2012) as Type I migration (Ida & Lin 2008; Bitsch et al. 2013), for light planets that migrate embedded in the disc; or Type II migration, for massive planets that open a gap in the disc. In this paper, we are interested in Type II migration (e.g. Lin, Papaloizou & Kley 1993; Syer & Clarke 1995; Ivanov, Papaloizou & Polnarev 1999), which can be further split into two regimes, defined through the local disc to planet mass ratio

$$B_0 = \frac{4\pi \Sigma_0 r^2}{m_\mathrm{p}}. \tag{1}$$

The 'disc-dominated' regime is defined as the regime where the local disc mass is higher than the planet mass; while the 'planet-dominated' regime, conversely, requires the planet to be more massive than the local disc.

The classical theory of the disc-dominated regime assumes that the planet is locked in the disc gap, with no possible flux of material crossing its orbit, and it migrates following the disc viscous evolution (e.g. Lin & Papaloizou 1979). In recent years, this simple picture has been questioned by hydrodynamics simulations' results; for example, Duffell et al. (2014) and Dürmann & Kley (2015) suggested that planet migration is unlocked from the disc viscous evolution and the planet can migrate faster than the disc material; other works (e.g. Lubow & D'Angelo 2006) modelled the gas flow through the planetary gap. A number of recent studies investigated the problem (e.g. Kanagawa, Tanaka & Szuszkiewicz 2018; Robert et al. 2018; Scardoni et al. 2020; Lega et al. 2021), and Scardoni et al. (2020) proposed that the hydrodynamic simulations mostly undergo a transient phase and over longer viscous time-scales the

★ E-mail: ces204@cam.ac.uk

planet migration conforms to the usual Type II picture; however, no definitive conclusion has been reached yet.

Strongly related to the migration problem is the study of the gap's properties, since most of the angular momentum is exchanged between the planet and the disc in proximity of the gap edges (Goldreich & Tremaine 1979, 1980); some important works analysing the gap shape and width are for example those by Crida, Morbidelli & Masset (2006), who provided an analytical formula linking the gap's and the planet–disc system properties; Fung, Shi & Chiang (2014), who analysed the expected density in the gap; and by Fung & Chiang (2016), who demonstrated that in 3D simulations, massive planets carve gaps whose properties are consistent with those produced in 2D simulations.

Regardless of the details of migration velocity in this regime, Type II migration is often suggested as an explanation for the existence of massive exoplanets characterized by small semimajor axes (the so-called hot Jupiters). Moreover, Type II migration in the planet-dominated regime – the main focus of this paper – might help in explaining the population of Jupiter-like planets located at larger radii. Indeed, in the latter regime, the planet's inertia is supposed to have a crucial impact on migration, slowing it down significantly.

The very first papers exploring this problem (Syer & Clarke 1995; Ivanov et al. 1999) studied the problem in 1D under the assumption that no material can cross the planet's location. Since the planet migrates more slowly than the local viscous velocity and the material cannot cross the gap, the fate of the inner disc is to disappear, as it is rapidly accreted by the central star. For the same reason, the gas located in the outer disc tends to accumulate at the outer gap edge. As the surface density of the gas at the outer gap edge increases, the torque pushing the planet inwards is enhanced, until reaching an equilibrium, where the planet moves at a rate matching the inward motion of the density maximum.

More recent studies have analysed the planet-dominated regime in different conditions, finding that in some circumstances the planet migration is not only slowed down, but even reversed. Crida & Morbidelli (2007), for example, studied the problem in the presence of a gap with a non-negligible amount of material. Adding the corotational torque in their computations, they found that it can have a significant influence on planet migration: if the Reynolds number is low enough the planet migrates outwards instead of inwards towards the star. Under the assumption that the planet migration is locked to the viscous evolution, another situation for potential outward migration is the case that the planet is initially located in the disc area which is viscously expanding (Veras & Armitage 2004). Hallam & Paardekooper (2018) instead showed that, under certain circumstances, the illumination of the outer gap edge by the central star's radiation can lower the torque exerted by the outer disc on the planet; they thus suggested that this is a possible mechanism to slow down or even reverse massive planet migration.

Further investigation on the planet migration direction has been recently conducted by Dempsey, Lee & Lithwick (2020) and Dempsey, Muñoz & Lithwick (2021), who used a set of 2D systems in the planet-dominated regime, in a stable steady state condition. To study planet migration they model the situation where the planet's orbital parameters (semimajor axis and eccentricity) are not allowed to evolve; they then calculate planet migration from the torques acting on the fixed planet. Since the planet cannot react to the disc either in a_p or in e_p, the migration rate for given system parameters is just proportional to the disc mass; migration is parametrized in terms of $\Delta T/(\dot{M} l_p)$, where ΔT is the torque acting on the planet, $\dot{M}$ is the steady state accretion rate, l_p is the specific angular momentum of the planet. Through their study, they found that for typical disc parameters, Jupiter-like (or lighter) planets migrate inwards, while super-Jupiter planets migrate outwards; interestingly, the sign of the torque (and thus direction of migration) seems to be related to the gap parameter $K' = q^2/(\alpha h^3)$ (which controls the gap depth; Kanagawa et al. 2016), where $q = m_p/M_*$ is the planet to star mass ratio, α is the Shakura & Sunyaev 1973 viscosity parameter, and $h = H/r$ is the disc aspect ratio. The parameter K' is a variant of the gap depth parameter $K = q^2/(\alpha h^5)$, which can be defined from the study of the torques' balance (see for example Fung et al. 2014; Kanagawa et al. 2015, 2018). Being proportional to the planet's gravitational torque ($\propto q^2/h^3$) and inversely proportional to the disc's viscous torque ($\propto \nu \propto \alpha h^2$), it can be interpreted as a measure of the relative strength of the torques.

These interesting results, however, are limited by the assumption of a fixed planet. Albeit in a different migration regime ($B > 1$, see equation 1), Scardoni et al. (2020) showed that when the planet is allowed to change its orbital parameters, the disc density readjusts to the presence of the moving planet, which modifies the disc-planet interaction. Although the two migration regimes cannot be directly compared, this work highlights the potential importance of including the evolution of the planet orbital parameters in the computation of disc-planet torques. The importance of the gap-adjustment due to planet migration in determining the evolution of the planet orbital parameters has recently also been underlined also by Lega et al. (2021). Furthermore, in live planet simulations, the torque exerted on the planet by the disc modifies both the semimajor axis and the eccentricity (e.g. Kley & Dirksen 2006; Duffell & Chiang 2015; Teyssandier & Ogilvie 2016; Rosotti et al. 2017; Ragusa et al. 2018), potentially producing a non-trivial relation between the torque and planet migration.

Another fundamental aspect of planet–disc interaction is the long time-scale over which the disc re-adjusts itself to the presence of the planet; in fact, although the time-scale of tidal interaction is short, the disc structure change might happen over the significantly longer viscous time-scale (e.g. Lin & Papaloizou 1979; Ward 1998). The importance of considering the long-term evolution of planet–disc systems has been demonstrated by Ragusa et al. (2018), who showed that the long term evolution obtained from hydrodynamic simulations can differ from the trend at the first stages of evolution. Apart from their work – which was mainly focused on the eccentricity evolution – no long-term migration studies in the $B < 1$ regime have been conducted with a 'live' (i.e. evolving) planet.

In this paper, we present a suite of 2D simulations lasting $\gtrsim$300k orbits, for a variety of aspect ratios H/r, planet masses M_p, and disc masses M_{disc}. These simulations are intended to be complementary to those by Dempsey et al. (2021), and allow us to investigate both the importance or otherwise of employing a 'live' planet, as well as the role of different boundary conditions. Since these simulations are extremely expensive from the computational point of view, such simulations have never been performed before; consequently, this is a new area of exploration for the disc–planet interaction problem, and the present simulation set inevitably leaves some questions unanswered. Nevertheless, they provide an intriguing starting point for further exploration in the field.

The paper is organized as follows: in Section 2, we describe the long numerical simulations performed to study planet–disc interaction; Section 3 contains the description of the planets' orbital parameters, and the analysis of the torques resulting from the disc to planet interaction; in Section 4, we discuss the influence of boundary conditions on the obtained torques on the planet; a toy model exploring the secular evolution of planets is developed in Section 5, and in Section 6 we discuss the implications of this

Table 1. Simulation parameters. The name of each simulation is chosen in the following way: 'L' or 'M' to indicate a light or massive disc, respectively; 'm' followed by a number to indicate the planet mass (measured in Jupiter masses); 'h' followed by a number to indicate the aspect ratio.

Name	B_0	m_p (m_J)	h_0	r_{in}	r_{out}	α_0	K_0'	K_0	N_{orbits}
L-m1-h036	0.046	1	0.036	0.2	15	0.001	21	1.65×10^4	6×10^5
L-m3-h036	0.046	3	0.036	0.2	15	0.001	193	1.49×10^5	3×10^5
L-m13-h036	0.046	13	0.036	0.2	15	0.001	3622	2.9×10^6	3×10^5
L-m13-h06	0.046	13	0.06	0.2	15	0.001	782	2.17×10^5	3×10^5
L-m13-h1	0.046	13	0.1	0.2	15	0.001	169	1.69×10^4	3×10^5
L-m1-h06	0.046	1	0.06	0.2	15	0.001	5	1.29×10^3	6×10^5
M-m1-h036	0.15	1	0.036	0.2	15	0.001	21	1.65×10^4	6×10^5
M-m3-h036	0.15	3	0.036	0.2	15	0.001	193	1.49×10^5	6×10^5
M-m13-h036	0.15	13	0.036	0.2	15	0.001	3622	2.9×10^6	3×10^5
M-m13-h06	0.15	13	0.06	0.2	15	0.001	782	2.17×10^5	3×10^5
M-m13-h1	0.15	13	0.1	0.2	15	0.001	169	1.69×10^4	3×10^5
M-m1-h06	0.15	1	0.06	0.2	15	0.001	5	1.29×10^3	$6 \cdot 10^5$

model for planetary demographics; finally, in Section 7 we draw our conclusions.

2 SIMULATIONS

2.1 Simulation parameters

We performed 12 2D hydrodynamical simulations of protoplanetary discs containing a massive planet with the grid code FARGO 3D (Benítez-Llambay & Masset 2016), considering a cylindrical reference frame (r, φ) centred in the star. We adopt dimensionless units $G = M_* = r_0 = 1$, where G is the gravitational constant, M_* is the star mass, and r_0 is the planet's initial location; the time unit is the inverse Keplerian frequency at r_0, Ω_k^{-1}; this means that the planet at its initial location r_0 requires $t = 2\pi$ to complete an orbit. Each simulation is run for 300k orbits or 600k, depending on the status of the steady state; the requirement is that $\dot{M}(r)$ is within 10 per cent of $\dot{M}(r_{in})$ at least until $r = 2.5\, a_p$.

The set-up for the simulations is defined in analogy with the simulations by Ragusa et al. (2018).[1] We consider logarithmically spaced $N_r = 430$ cells in the radial direction, from $r_{in} = 0.2$ to $r_{out} = 15$, and linearly spaced $N_\varphi = 580$ cells in the azimuthal direction, extending from 0 to 2π. We assume a locally isothermal equation of state set by equation (3), and we parametrize the viscosity by applying the α prescription by Shakura & Sunyaev (1973), $\nu = \alpha c_s H$, with α defined as a function of radius

$$\alpha = \alpha_0 r^{-0.63}; \tag{2}$$

in all the simulations we fix $\alpha_0 = 0.001$.

In our simulations, we consider a variety of disc aspect ratios and planet masses. Specifically, we consider flared discs, defining the aspect ratio as follows:

$$h = H/r = h_0 r^{0.215}, \tag{3}$$

where h_0 is the aspect ratio at the initial planet location, for which we consider three different values ($h_0 = 0.036, 0.6$, and 0.1). Regarding the planet mass, we explore three different values: $m_p = 1\, m_J$, $m_p = 3\, m_J$, and $m_p = 13\, m_J$.

For each combination of parameters h_0 and m_p, we perform two simulations, characterized by different values for the initial local disc to planet mass ratio B_0 (see equation 1). The initial disc surface density at planet location Σ_0 is chosen to obtain the selected values for the initial value B_0; we thus have 'massive' disc simulations, with $B_0 = 0.15$, and 'light' disc simulations, with $B_0 = 0.046$. Note that in physical units, $B_0 = 0.046$ and $B_0 = 0.15$ for a Jovian mass planet at the radius of Jupiter corresponds to a local disc surface density of 1.3 and 4.2 g/cm^2, respectively. Apart from m_p, h_0, and Σ_0, all the other parameters are kept fixed among all the simulations. Being interested in the planet-dominated regime of Type II migration, we only considered values $B_0 < 1$; for planet migration with high B values we refer to our previous study (Scardoni et al. 2020), specifically focused on the disc-dominated regime of Type II migration.

In addition to the simulations outlined in Table 1, we performed two high resolution simulations as convergence test: we performed simulations L-m13-h036 and M-m13-h036 with $\times 2$ and $\times 4$ the standard resolution used in this paper, and verified that the obtained orbital parameters are the same as those obtained using the standard resolution.

2.2 Initial and boundary conditions

The initial density profile is defined as

$$\Sigma(r) = \Sigma_0 r^{-0.3} \times e^{(-r/5)^{1.7}}. \tag{4}$$

The planet mass is gradually increased during the first 50 orbits of the simulation, while its orbital parameters are kept fixed; once the planet reaches its full mass, it is allowed to evolve (i.e. to migrate and develop eccentricity) under the action of torques arising from planet–disc interaction.

We apply closed boundary conditions at the outer edge $r_{out} = 15$ by setting both the velocity and the gas density to zero at r_{out}, i.e. no material is added to the simulation, in order to minimize the effect of the outer boundary condition. This generates a zero flux at r_{out}, which physically corresponds to the case of a disc truncated by a wide binary. At the inner boundary, instead, we apply 'viscous' boundary conditions, i.e. we enforce the inner material velocity to match the viscous velocity (as in Scardoni et al. 2020 and Dempsey et al. 2020, 2021). This choice ensures that the inner boundary has a net zero effect on the total angular momentum budget of the disc, i.e. the torque supplied exactly matches the rate of angular momentum advected by accretion through the inner boundary.

In practice, the simulations are run for a small fraction of the viscous time-scale at the outer edge so that the form of the outer

[1] In turn, their choice of parameters was based on the best fit for CI Tau disc by Rosotti et al. (2017).

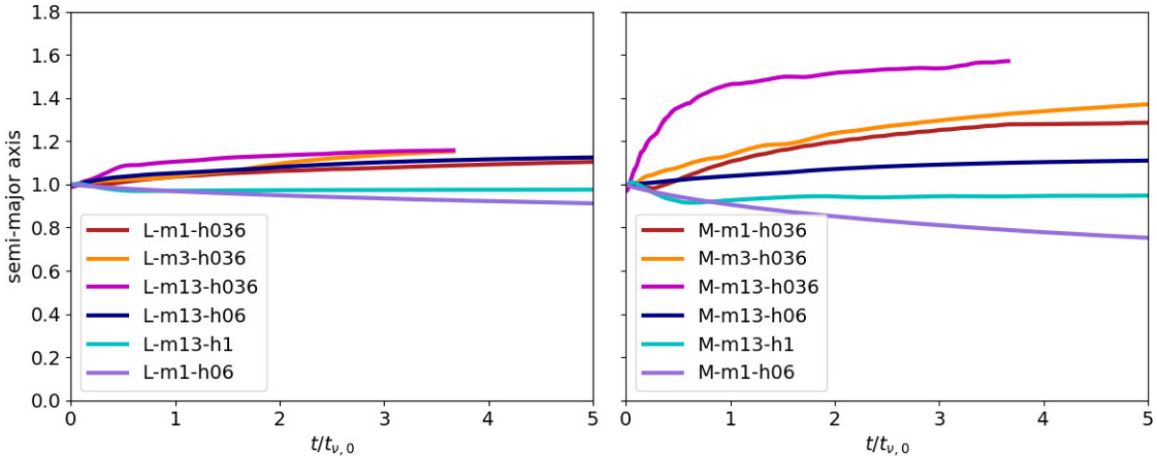

Figure 1. Semimajor axis as a function of the evolutionary time for light disc simulations (left-hand panel) and massive disc simulations (right-hand panel). The different colours correspond to different simulations, as indicated in the plot legend (see Table 1 for the simulations' name definition).

boundary should not be critical to the calculations. On the contrary, boundary effects can disturb the inner disc and thus the region around the planet on much shorter time-scales, due to spurious wave propagation. We therefore employ the wave damping method by de Val-Borro et al. (2006) for the radial velocity at the inner boundary. This means that over the damping time-scale ($\tau = \Omega_k/30$), we damp v_r to the azimuthal average of the initial (viscous) velocity $\langle v_{r,0}\rangle$ in the region from $r_{\rm in}$ to $r = 0.3$.

We also perform an additional simulation characterized by the same parameters as simulation L-m13-h036, except for the inner radius and damping zone, which are taken to be half of the default values; thus, we take $r_{\rm in} = 0.1$, and the damping zone extends in this case up to $r = 0.15$. This is to ensure that in the cases where the planet develops high eccentricity (and thus gets close to the inner boundary), the material in the damping zone does not affect the migration owing to numerical modification to the physical torque exerted on the planet.

3 RESULTS

3.1 Orbital parameters

In Fig. 1, we show for the light disc simulations (left-hand panel) and the massive disc simulations (right-hand panel) the evolution of the semimajor axes as a function of evolutionary time, i.e. the physical time rescaled to the viscous time-scale at the initial planet position

$$t_\nu = \frac{2}{3}\frac{r^2}{\nu}, \tag{5}$$

and we indicate with $t_{\nu,0}$ the viscous time-scale evaluated at the initial planet location. For reference, the initial viscous time-scales in our simulations are: $t_{\nu,0} \sim 9 \times 10^5$ yr for $h = 0.036$, $t_{\nu,0} \sim 3 \times 10^5$ yr for $h = 0.06$, $t_{\nu,0} \sim 10^5$ yr for $h = 0.1$. After an initial adjustment (lasting $t \lesssim t_{\nu,0}$), we can notice a variety of behaviours: inward migration (e.g. L-m1-h06, M-m1-h06), outward migration (e.g. L-m13-h036, M-m3-h036), or even stalling (e.g. L-m13-h1, M-m13-h06). This interesting behaviour can be related to the value of the gap-opening parameter $K' = q^2/(\alpha h^3)$ (where $q = m_{\rm p}/M_*$), whose analysis is deepened in Section 3.2.

Fig. 2, instead, illustrates the planet eccentricity evolution. This plot shows a variety of behaviours, with some simulations (especially at higher planet masses) exhibiting significant eccentricity growth. It is also worth noticing that, in many cases, the planet eccentricity presents oscillations (as already observed, for example, by Duffell & Chiang (as already observed, for example, by Duffell & Chiang 2015; Rosotti et al. 2017; Thun, Kley & Picogna 2017; Ragusa et al. 2018). These oscillations are due to the disc eccentricity vector evolving as a superposition of two rigidly precessing normal modes (Teyssandier & Ogilvie 2016, 2017; Ragusa et al. 2018; Teyssandier & Lai 2019).

3.2 Torques

3.2.1 Dependence on initial disc mass

In this section, we analyse the torque acting on the planet as a function of the following parameter (Kanagawa et al. 2015)

$$K' = \frac{q^2}{\alpha h^3}, \tag{6}$$

which is a modification of the gap-opening parameter $K = q^2/(\alpha h^5)$, i.e. a measure of the strength of the planet's gravitational torque ($\propto q^2/h^3$) compared to the disc's viscous torque ($\propto \nu \propto \alpha h^2$).

The parameter K' has been empirically studied by Kanagawa et al. (2016, 2018) and Dempsey et al. (2020, 2021), who noticed that K' correlates with the gap width and depth (with the gap becoming wider and deeper for higher K' values). Systems characterized by the same K' also appear to show similar torque density profiles; thus Dempsey et al. (2020, 2021) examined a number of fixed-planet[2] simulations characterized by different K' values, and suggested that K' is a good 'ordering parameter' for planet migration. According to their analysis, in fact, planets in systems characterized by $K' \gtrsim 20$ migrate outward, whereas systems with $K' \lesssim 20$ present inward planet migration. Since their finding relies on simulations characterized by an evolving disc and fixed planets, our goal is to test whether the torque imposed on a fixed planet on a circular orbit is the same that applies in the case of a 'live' planet that can respond to the torque during the evolution by changing its orbital elements.

For this purpose, we follow the approach of Dempsey et al. (2021), and plot the total torque on the planet normalized to $\dot{M} l_{\rm p}$ (see their

[2]In fixed-planet simulations, the torque on the planet is computed as integration of the torque arising from the disc, from which planet migration is deduced; none the less, the planet orbital parameters are kept fixed at their initial values (i.e. $a_{\rm p} = 1$, $e_{\rm p} = 0$).

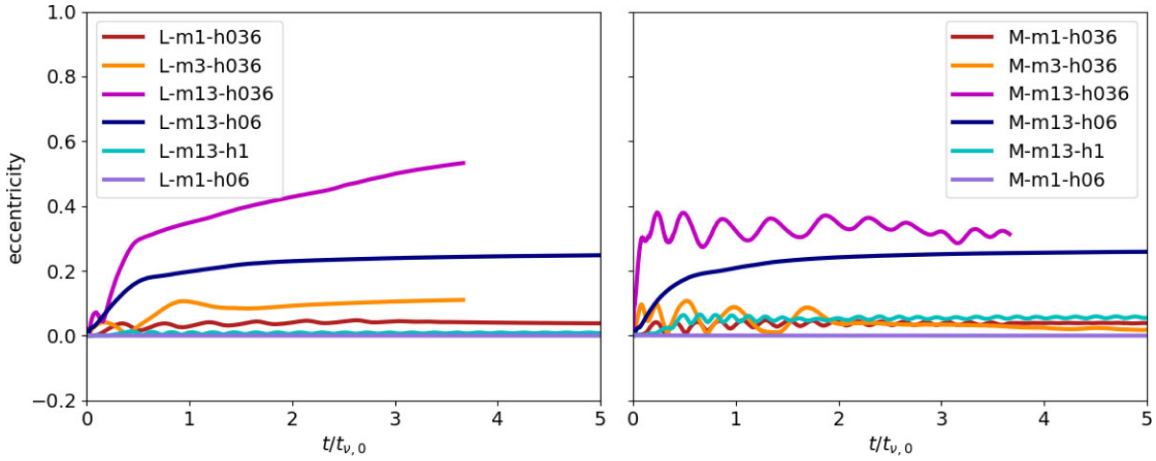

Figure 2. Eccentricity as a function of the evolutionary time for light disc simulations (left-hand panel) and massive disc simulations (right-hand panel). The different colours correspond to different simulations, as indicated in the plot legend (see Table 1 for the simulations' name definition).

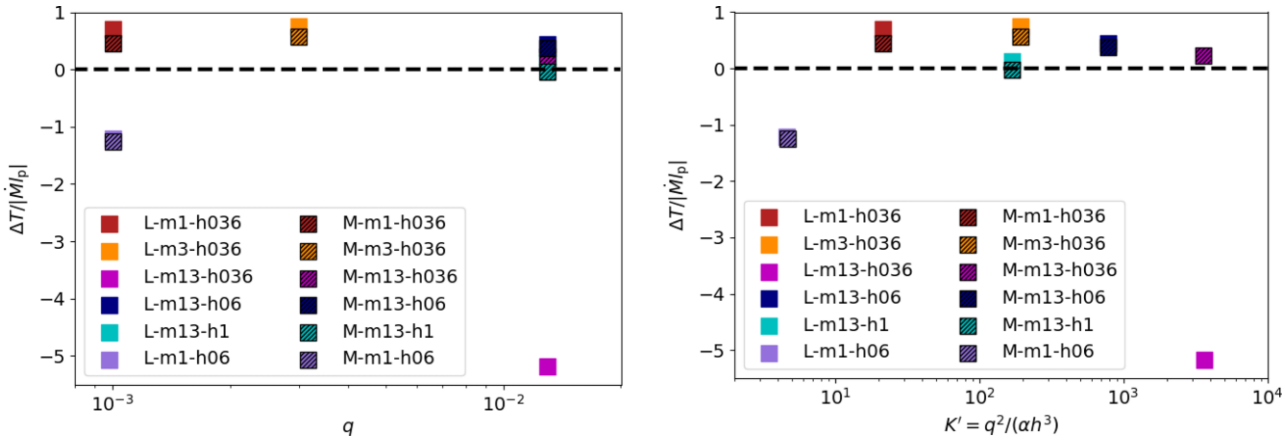

Figure 3. Torque acting on the planet normalized for the VSS accretion rate times the local specific angular momentum as a function of q (left-hand panel) and parameter $K' = q^2/(\alpha h^3)$ (right-hand panel). The squares indicate the torque acting computed as variation rate of the planet's angular momentum obtained from the simulations; the different colours correspond to different simulations, as indicated in the legend.

fig. 2). Note that for our convention of signs we have $\dot{M} < 0$ for inward migration; to avoid confusion we therefore plot $\Delta T/|\dot{M}l_p|$ whose sign only depends on the sign of the torque exerted by the disc on the planet (positive for outward migration and negative for inward migration).

The presence of a live planet enables us to compute the torque acting on the planet directly as the planet's angular momentum variation rate

$$\Delta T = \frac{\mathrm{d}J_p}{\mathrm{d}t} = J_p \left(\frac{1}{2a} \times \dot{a} - \frac{e}{1-e^2} \times \dot{e} \right), \tag{7}$$

being $J_p = m_p \sqrt{GM_* a_p (1-e_p^2)}$. Thus, we compute ΔT time-averaged over 30 000 planet orbits,[3] taken in the last stages of the simulation, when the inner disc has reached a steady state and the planet migration has stabilized. The results are shown in Fig. 3, from which we can notice that the general trend of positive torques for high K', and negative torques for low K' is confirmed, albeit with a suggestion of some decline in the torque at values of $K' > 20$–200. Note, however, that the suite of simulations performed so far does not explore the K' values extensively enough to confirm that $K' = 20$ is the point of zero torque, and further simulations are needed for a precise characterization of the ΔT–K' relation.

We further notice an applicability limitation in the results obtained from fixed planet simulations by Dempsey et al. (2020, 2021). Those simulations do not conserve the total angular momentum of the system, because they do not allow the planet to evolve its orbital parameters. Although this approach is completely adequate to represent the limiting behaviour in the case that $B_0 \to 0$ (for which the planet is not expected to modify its orbital parameters noticeably over the disc lifetime), it cannot necessarily be used for $B_0 \neq 0$ studies, where the planet might change its orbital parameters over the simulation time-scale, and in the process affects the interaction with the disc. This limitation becomes evident when we compare our results for different B_0 values (i.e. 'light disc' versus 'massive disc'), where we notice that the normalized torque properties change for different B_0 values in some cases. In the approach adopted by Dempsey et al. (2021), by contrast, both the torque and the accretion rate are assumed to vary linearly with B_0 and hence their ratio is independent of B_0; therefore, in Dempsey et al. (2020, 2021) simulations the torque applied to the planet is, by construction, proportional to the disc mass.

[3] 30 000 orbits was chosen as being several times the time-scale for periodic exchange of eccentricity between the planet and the disc, this being modulated on the beat period between the precession of the aligned and anti-aligned eccentric modes of the disc.

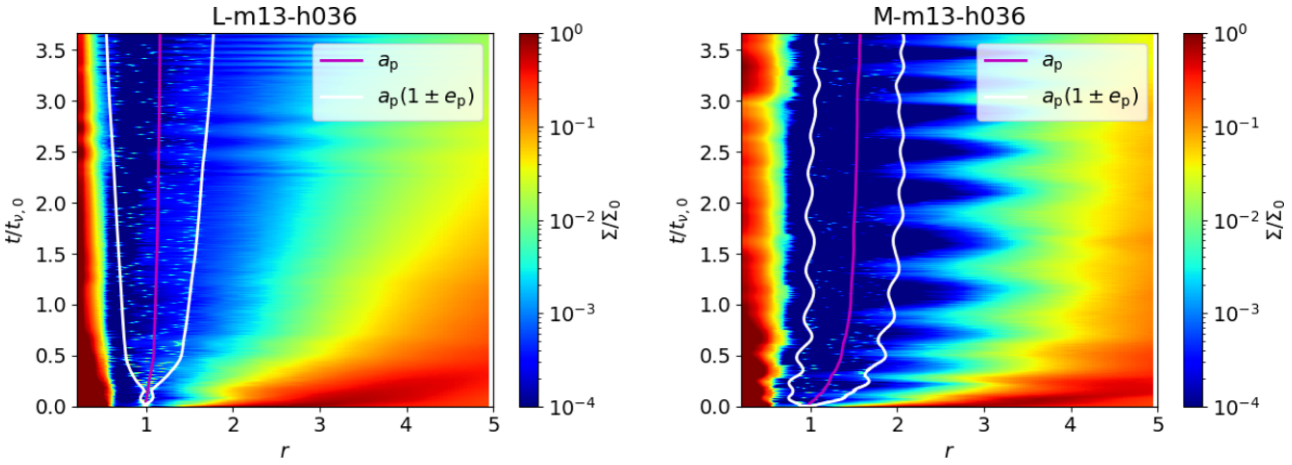

Figure 4. Azimuthal averaged density profiles Σ/Σ_0 (colour map) as a function of the radius (x-axis) and time normalized to the viscous time-scale at the initial planet location (y-axis). The magenta line shows the time evolution of the planet's semimajor axis; the white lines show the time evolution of $a_p(1 \pm e_p)$. The left-hand panel refers to simulation L-m13-h036; the right-hand panel refers to simulation M-m13-h036.

Our simulations demonstrate instead that although the assumption of torques independent of the disc mass is adequate for low mass planets, it breaks down in the case of high K' ($>10^3$).

We find that the normalized torque values are indeed approximately independent of B_0 in the case of the Jovian mass planet (see Fig. 3) but that for higher values of planet mass (and K') the normalized torque values become increasingly divergent between the 'light' and 'massive' simulations. This is particularly marked in the case of the simulation with the largest K' value (the 13 m_J planet with the lowest disc aspect ratio). These results can be readily understood from Fig. 2 where it can be seen that the planet develops significant eccentricity during the course of the simulation. As discussed by Ragusa et al. (2018) and Teyssandier & Lai (2019), the eccentricity evolution of the planet depends on the interplay between eccentric modes of the disc whose structure depends on the disc to planet mass ratio. Thus, we see in Fig. 2 that not only do the simulation with largest K' develop large eccentricities but that the eccentricity evolution is markedly different in the 'light' and 'massive' cases. It is therefore unsurprising that the torques on the planet evolve differently; indeed, in the light case, the eccentricity grows to the point where although the semimajor axis increases, the torque on the planet is actually negative (Fig. 3), a result that is reconciled by the large planetary eccentricity in this case. We could thus consider simulation L-m13-h036 as an 'outlier' in Figs 3 and 7 because it is the extreme case where the torque mainly affects e_p rather than a_p.

The different evolutionary histories of the disc structure in the light and massive 13 m_j case are illustrated in Fig. 4 (in the left-hand and right-hand panel, respectively). The strong growth of planetary eccentricity in the light case is associated with the system settling into a single eigenmode of the system, i.e. the slow mode in which the apsidal precession of the disc and planet are aligned. In the massive case, conversely, the system exists in a state of superposition of aligned and anti-aligned modes (see Ragusa et al. 2018, for more discussion on the two modes), resulting in the modulation of planetary eccentricity and disc structure evident in Figs 2 and 4.[4]

We therefore conclude that the results based on non-migrating planet simulations presented by Dempsey et al. (2020, 2021) are a good approximation for light planets; none the less a more complex model, accounting for the planet's eccentricity growth and its dependence on disc mass, is needed when higher mass planets are considered.

Finally we emphasize that Fig. 3 is constructed after significant evolution of the disc profiles (i.e. after 6×10^5 planetary orbits in the case of the massive and light simulations with 1 m_j planet, and in the massive disc simulation with 3 m_j planet; and after 3×10^5 planetary orbits in the remaining simulations) and use values of the torque and accretion averaged over the preceding 3×10^4 orbits. The result that the simulations with higher K' values generally result in normalized torque values that are $\sim$0.5 is all the more remarkable given the substantial variety in the surface density evolution that occurs in the various simulations. This is illustrated in Fig. 5 which shows snapshots of the surface density profiles (as a function of radius normalized to the current semimajor axis of the planet) in each of the simulations at the time that the normalized torques shown in Fig. 3 are evaluated. In each case, the solid and dashed versions of the curves relate to corresponding pairs of simulations with different values of B_0. The density is normalized to the initial surface density at the location of the planet in the unperturbed disc and therefore the relative surface density in each simulation pair can be obtained by scaling with the relevant values of B_0 for the light and massive disc simulations.

Fig. 5 demonstrates that it is only in the case of the simulation pair (L-m1-h06 and M-m1-h06) with lowest K' (i.e. narrowest gap) that the surface density profiles are simply scaled versions of each other. This can be traced to the fact that the planetary eccentricity is not excited in this case (see Fig. 2) as can be expected in the case of a narrow gap where corotation torques dominate over Lindblad resonances (Goldreich & Tremaine 1979, 1980). At the other extreme, the simulations where the planetary eccentricity is most excited (i.e. the m13-h036 and m13-h1 pairs) show that the inner edge of the planet carved cavity is close to the 3:1 inner eccentric

[4]In the light disc case with 13 m_j planet, the planet achieves such a high eccentricity that the pericentre distance is only $\sim$2.5 times the inner disc edge, r_{in}. In order to check that the location of the inner boundary is not driving the evolution in this case, we have re-run the light disc case with r_{in} reduced by a factor 2–0.1. We show in Appendix A that the evolution of the planetary orbital elements is unaffected by the reduction in r_{in}.

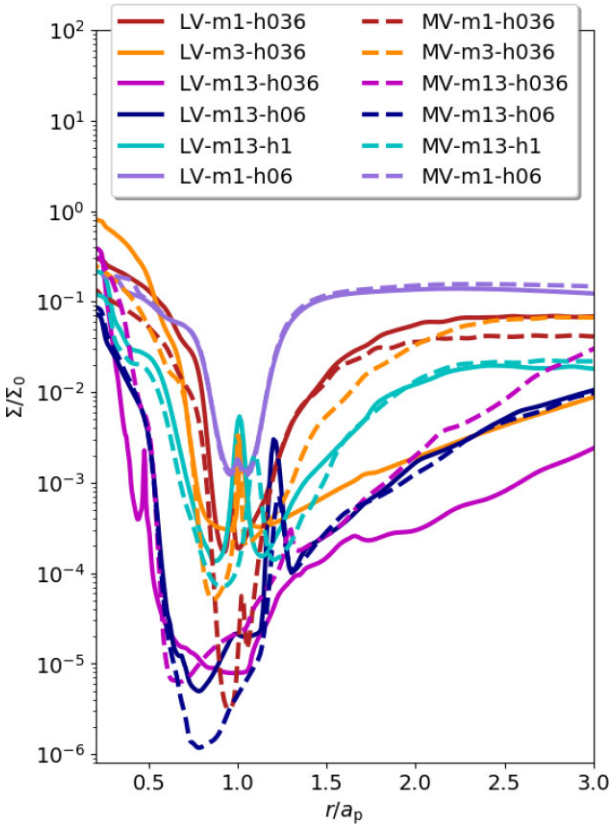

Figure 5. Azimuthal averaged density profiles Σ/Σ_0 (colour map) at the end of the simulation time, plotted as a function of the radius normalized to the planet location (both the density profile and the planet location are taken at the final snapshot of each simulation). Each colour refer to a different simulation, as indicated in the legend; the light and massive disc simulation with the same planet mass and disc aspect ratio are shown with the same colour with solid and dashed lines, respectively.

Lindblad resonance which is associated with strong driving of orbital eccentricity (Lin et al. 1993; Goldreich & Sari 2003).

We note that, in contrast to the simulations of Dempsey et al. (2020, 2021), we do not drive the accretion rate at a prescribed rate in these simulations; the accretion rate at the inner edge (which is applied to the calculation of the normalized torque in Fig. 3) evolves rapidly during the first viscous time-scale at the planetary radius, thereafter setting up a quasi-steady state within a few times the planetary radius (e.g. see Fig. 10). Thereafter, the magnitude of the accretion rate declines on the viscous time-scale at the half mass radius of the disc, as expected. It is this slow decline in the accretion rate in the inner disc (and the associated normalization of the surface density) that drives the levelling off in the evolution of the semimajor axis seen in Fig. 1. In Section 5, we will explore toy models which use the normalized torque values extracted from our simulations to calculate the secular evolution of planets in an evolving disc.

3.2.2 *Torque components*

So far, we have evaluated the total torque on the planet, including contributions from both rate of change of semimajor axis and rate of change of eccentricity, as in equation (7). In Fig. 6, we plot instead the torque component associated with the rate of change of only the

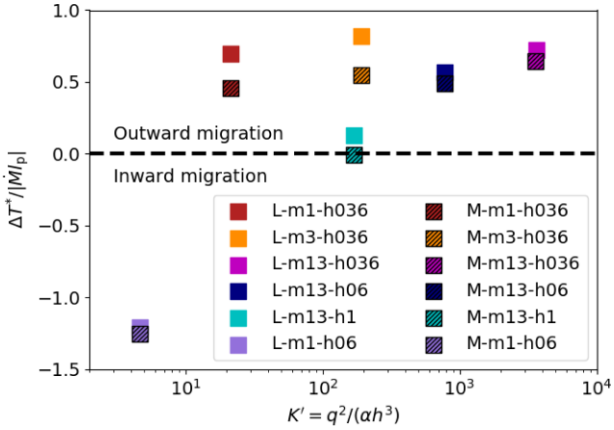

Figure 6. Torques associated with the rate of change of semimajor axis normalized for the VSS accretion rate times the local specific angular momentum as a function of parameter $K' = q^2/(\alpha h^3)$. The different colours correspond to different simulations, as indicated in the legend.

semimajor axis against the parameter K'

$$\Delta T^* = \frac{m_\mathrm{p}}{2} \times \sqrt{\frac{GM_*}{a_\mathrm{p}}(1-e_\mathrm{p}^2)} \times \dot{a}_\mathrm{p}. \tag{8}$$

We notice that in this case there is little difference between the torques associated with $\dot{a}_\mathrm{p}$ for the light and massive disc simulations with 13 m_j and $h = 0.036$. This suggests that the differences in total torque between these two simulations do not result from interactions that transfer significant orbital energy to the planet, but are instead associated with interactions that primarily affect the planetary eccentricity.

We furthermore notice that at large K' (or K, see the next section), the normalized ΔT^* is almost constant with K' (or K), whereas ΔT seems to decrease. This behaviour suggests that as the planet mass increases, the resonances that excite/damp the planet's eccentricity are strengthened/weakened; while the resonances responsible for migration seem less affected.

This result has interesting implications on the rate of energy transfer to the planet. Given that in this case the variation of normalized ΔT^* between simulations is much less than if the total normalized torque is considered, even the L-m13-h036 simulation (where the total normalized torque is large and negative: see Fig. 2) has a positive normalized ΔT^* value whose magnitude ($\sim$0.5) is similar to that in lower mass planets. This implies that the spread in normalized ΔT values for the most massive planets is driven by differences in eccentricity evolution which are not associated with significant contributions to the transfer of energy between disc and planet. Given that

$$E_\mathrm{p} = -\frac{GM_*m_\mathrm{p}}{2a_\mathrm{p}}, \tag{9}$$

the rate of change of planetary orbital energy is given by

$$\dot{E}_\mathrm{p} = \frac{GM_*m_\mathrm{p}}{2a_\mathrm{p}^2}\dot{a}_\mathrm{p}. \tag{10}$$

Combining equation (10) and the torque associated with the semimajor axis variation $|\Delta T^*|$ (equation 8), we deduce that

$$\dot{E}_\mathrm{p} = \left(\frac{\Delta T^*}{\dot{M}l_\mathrm{p}}\right) \times \left(\frac{GM_*}{a_\mathrm{p}}\right) \times \dot{M}. \tag{11}$$

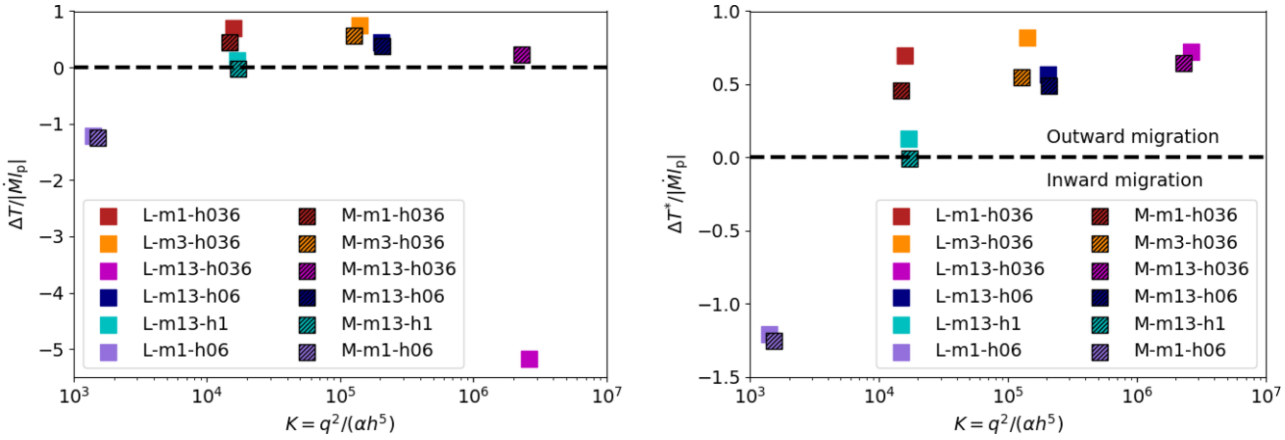

Figure 7. Left-hand panel: torque acting on the planet normalized for the VSS accretion rate times the local specific angular momentum as a function of K. Right-hand panel: torques associated with the rate of change of semimajor axis normalized for the VSS accretion rate times the local specific angular momentum as a function of K. The different colours correspond to different simulations, as indicated in the legend.

Since from our simulations the normalized ΔT^* is roughly constant (right-hand panel in Fig. 7), equation (11) implies that the energy transfer to the planet at a given location depends only on the accretion rate through the disc and is independent of planet mass.

Moreover, we note that the migration rate, $\dot{a}_p$, scales with $\dot{M}/m_p$ and, for simulations with the same value of B_0 and t_v, should be independent of planet mass. This can be seen from the asymptotic gradients of the migration tracks shown in Fig. 1.

The analysis of the torque components allowed us to attribute the deviation of the torques ΔT from the constant value at high K (or K') to the planet eccentricity excitation, and we noticed that the effect becomes more and more important as K (K') increases. We plan to further explore the behaviour at high K (or K') in future works.

3.2.3 *Choice of ordering parameter*

The torque analysis conducted so far is following Dempsey et al. (2020, 2021) in assuming that K' is the appropriate ordering parameter. In Fig. 7, we instead plot the normalized torques as a function of

$$K = \frac{q^2}{\alpha h^5} \tag{12}$$

for all our simulations, considering both the total torque (left-hand panel) and the torque associated with $\dot{a}_p$ (right-hand panel). While the number of simulations is too small to make a definitive judgement on the parameter that best captures the transition between narrow gaps with inward migration and broad gaps with outward migration, Fig. 7 suggests that this transition occurs at $K = 1.5 \times 10^4$. We use this threshold in our 'toy modelling' presented in Section 5. Remarkably, the normalized torque associated with $\dot{a}$ assumes a constant value of $\sim$0.5 for higher values of K.

4 ROLE OF INNER BOUNDARY CONDITIONS

In this section, we discuss the role of boundary conditions in planet migration simulations. For this purpose, we performed a set of additional simulations, characterized by the same parameters as those presented above, but with 'open' boundary conditions at the inner boundary. The open boundary conditions allow the material to leave the grid at the inner edge at its own radial velocity (numerically, we set both the velocity and the density in the inner ghost cell equal to the last active cell). As a consequence, at $r_{in} = 0.2$, we have a zero torque boundary condition, as illustrated in Fig. 8, where the viscous torque is shown as a function of r at different snapshots for simulation M-m3-h036 with open boundary conditions.[5]

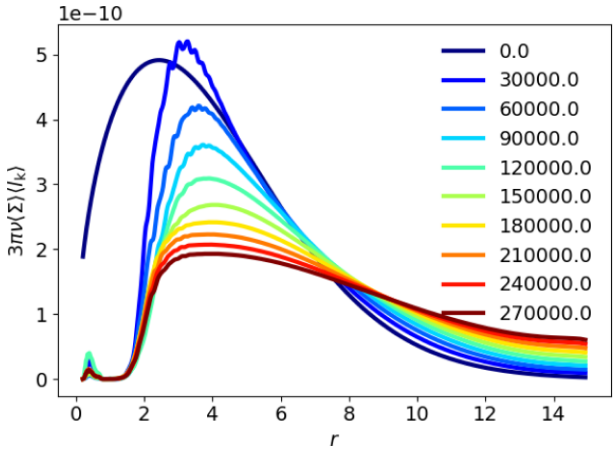

Figure 8. Viscous torque at different snapshots (showed in different colours, as indicated by the legend) for simulation M-m3-h036 with viscous boundary conditions.

From the physical point of view, the open boundary conditions produce a strong depletion of the inner disc; we can therefore apply them to study the physical case of a disc with a zero-torque inner cavity; for example, it may represent a case where the angular velocity is subject to a turning point (e.g. the classical boundary layer), or any case where material is removed from the cavity without injecting angular momentum to exterior material (e.g. photoevaporation or magnetospheric accretion).

The different physical configuration naturally produces differences in the migration properties that can be analysed in terms of $\Delta T^{in}/|\dot{M}l_p|$, where ΔT^{in} is the torque imparted to the planet from the disc interior to the planet. In order to analyse the different torques acting on the planet in the two cases, we commence by noticing that

[5] In this section, we use simulation M-m3-h036 as an example to illustrate the viscous torque and the accretion rate profile through the disc. Note, however, that the same behaviour is shown by all the other simulations in our sample.

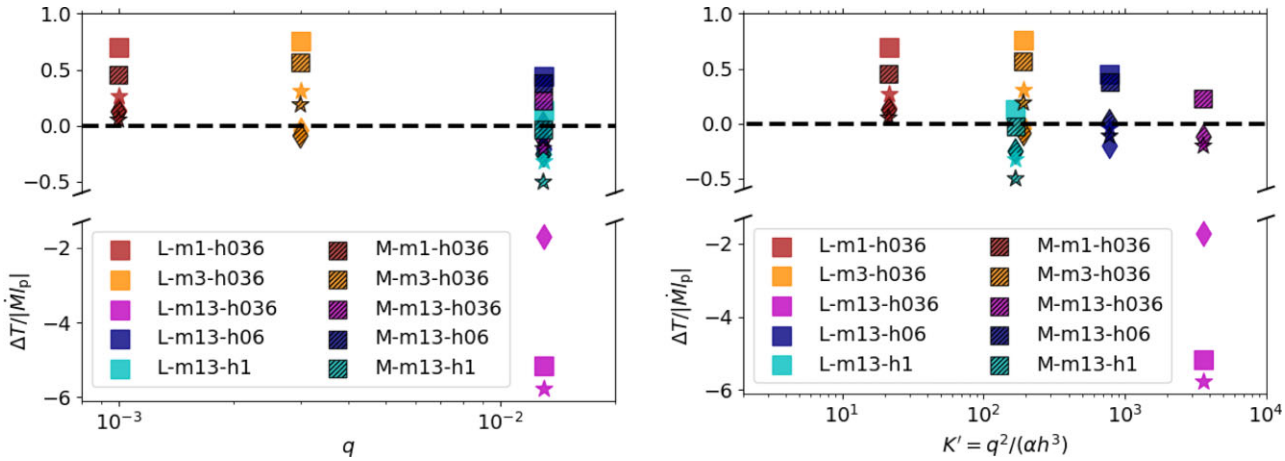

Figure 9. Torque acting on the planet normalized for the VSS accretion rate times the local specific angular momentum as a function of q (left-hand panel) and parameter $K^{'} = q^2/(\alpha h^3)$ (right-hand panel). The diamonds indicate the results from the open boundary condition simulations; the squares illustrate the torque the results from the viscous boundary condition simulations; the stars show the prediction for the open boundary condition results, applying equation (16) to the results obtained from viscous boundary conditions.

for both the boundary condition choices, the inner disc (from $r_{\rm in}$ to a few $r_{\rm p}$) reaches a viscous steady state after some $t_{\nu,0}$ (see Fig. 10). If we consider the area of the disc between $r_{\rm in}$ and $r_{\rm p}$, the total angular momentum injected per unit time into this region is due to advection and viscous torques at $r_{\rm in}$ and $r_{\rm p}$ is:

$$\Delta T^{\rm in} = -\dot{M}(l_{\rm p} - l_{\rm in}) + F_\nu(r_{\rm in}) - F_\nu(r_{\rm p}) \sim -\dot{M}(l_{\rm p} - l_{\rm in}) + F_\nu(r_{\rm in}), \quad (13)$$

where the approximation is valid for planets massive enough to create a deep gap in the disc, so that $\Sigma(r_{\rm p}) \sim 0$, and thus $F_\nu(r_{\rm p}) = 3\pi\nu\langle\Sigma\rangle\langle l_{\rm k}\rangle \sim 0$. Since for open boundary conditions $F_\nu(r_{\rm in}) \sim 0$, the torque in this case is

$$\Delta T^{\rm in}_{\rm open\ BC} = -\dot{M}(l_{\rm p} - l_{\rm in}); \quad (14)$$

whereas for viscous boundary conditions $F_\nu(r_{\rm in}) = -\dot{M} l_{\rm in}$, thus

$$\Delta T^{\rm in}_{\rm viscous\ BC} = -\dot{M} l_{\rm p}. \quad (15)$$

We can therefore estimate the difference in torque imparted by the inner disc

$$\Delta T^{\rm in}_{\rm open\ BC} = \Delta T^{\rm in}_{\rm viscous\ BC} + \dot{M} l_{\rm in}, \quad (16)$$

where $\dot{M} < 0$ (for our convention of signs), thus $\Delta T_{\rm viscous\,BC} > \Delta T_{\rm open\,BC}$. Since in both cases, the quasi-steady state of the inner disc requires that ΔT is balanced by the torque applied by the planet, it follows that the form of the inner boundary condition should alone determine the normalized torque of the inner disc on the planet. The overall physical consequence is that planets in discs with an inner cavity are expected to be less prone to outward migration than planets in discs where the angular momentum lost by advection is balanced by the viscous torque of inward lying material.

Using equation (16), we can predict the open boundary conditions' results from the values obtained for viscous boundary conditions (and vice versa). We illustrate the extent to which this simple prediction of how the inner boundary condition affects the planet migration through the plot in Fig. 9. In that plot, we show the torque acting on the planet (computed as time derivative of the planet angular momentum) for both the viscous boundary conditions (squares) and the open boundary conditions (diamonds). The stars, instead, show the prediction for the open boundary conditions' results, based on the viscous boundary conditions' results, using equation (16), and assuming that the inner boundary condition does not affect the torque on the planet from the outer disc. Each colour corresponds to a different simulation, which is indicated in the legend.

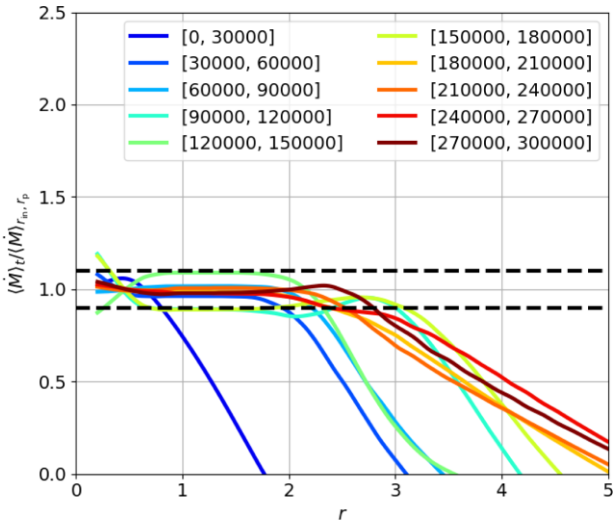

Figure 10. Normalized accretion rate profiles time averaged over different time intervals (in the legend, we indicate the initial and final orbit of the considered interval) for the massive disc simulation with $m_{\rm p} = 3\,m_{\rm j}$, $h = 0.036$ (M-m3-h036). The black dashed lines show the 10 per cent limits on the value of the normalized accretion rate, in order to consider the region in steady state.

Fig. 9 shows that for the 1 Jupiter mass simulations with $h = 0.036$, the difference in normalized torque is almost exactly that predicted by equation (16) (with $r_{\rm in} = 0.2$). Indeed, the outward migration is significantly slowed when a zero torque boundary condition is applied at $r_{\rm in} = 0.2$, because of the diminished torque delivered by the depleted inner disc. The prediction of equation (16) is appropriate as long as (a) the inner disc is in steady state interior to the planet (as assumed in the derivation of equation 16), and (b) the modification of the structure of the inner disc due to the changed boundary condition does not modify the torque exerted by the outer disc. This explains the quantitative agreement between the predictions of equation (16) and the change in total torque experienced by the planet shown in

Fig. 9 for simulations characterized by low-mass planets, where both the conditions are satisfied. We have verified, through examination of radial profiles of accretion rate (see Fig. 10), that the condition (a) is satisfied in all simulations. We therefore attribute the fact that the quantitative agreement with equation (16) declines as the planet mass increases to the breakdown of assumption (b). This is particularly evident in the case of the light $13m_j$ simulation with $h = 0.036$ where equation (16) fails to replicate the dependence of torque on boundary condition both in magnitude and in sign. It is notable that these parameters result in significant planetary eccentricity in the case of both boundary conditions but that the eccentricity growth is weaker in the case of the zero torque (cavity) boundary condition (compare Fig. 2 with fig. 6 of Ragusa et al. 2018). The modification of the outer disc structure in response to the different orbital evolution of the planet means that the difference in total torque is not simply related to the effect of the boundary condition on the inner disc alone.

5 EXPLORATION OF SECULAR EVOLUTION USING A TOY MODEL

In this section, we define a toy model that provides a simplified prediction of massive planets' migration, under the following key assumption: (i) $\Delta T/\dot{M}l_p$ is a function of K (equation 12); (ii) $\Delta T/\dot{M}l_p$ is independent of disc mass.[6] Since the disc is flared, we expect $K \propto h^{-5}$ to vary with radius as $K \propto r^{-5f}$, where f is the flaring index; in this section we assume constant α, but if we allowed it to vary with radius, it would have given a further contribution to the dependence of K on r.

We compute the planet migration time using the angular momentum definition $M_p l_p = M_p\sqrt{GM_* r_p}$[7]

$$t_{\rm mig} = \frac{r_p}{\dot{r}_p} = \frac{1}{2}\cdot\frac{M_p l_p}{\Delta T}, \tag{17}$$

where $t_{\rm mig} < 0$ (>0) means inward (outward) migration. Using the definitions $M_d = 4\pi r^2\Sigma$ and $\dot{M} = 3\pi\nu\Sigma$, we can rewrite the migration time-scale as

$$t_{\rm mig} = \frac{1}{2}\times\left(\frac{|\dot{M}|l_p}{\Delta T}\right)\times\left(\frac{M_p}{M_d}\right)\times\left(\frac{M_d}{|\dot{M}|}\right). \tag{18}$$

Noticing that $M_p/M_d = 1/B$ and $M_d/\dot{M} = t_\nu$,[8] this can be written as

$$\frac{r_p}{\dot{r}_p} = \frac{1}{2}\times\left(\frac{|\dot{M}l_p|}{\Delta T}\right)\times\left(\frac{t_\nu}{B}\right). \tag{19}$$

We now consider 3 different regimes:

(i) classical Type ii migration with $B \gg 1$, for which $r_p/\dot{r}_p = -t_\nu$, hence we deduce $\Delta T/\dot{M}l_p = -0.5/B$ (see for example Lin & Papaloizou 1979; D'Angelo, Bate & Lubow 2005; Scardoni et al. 2020);

(ii) classical Type ii migration with $B \ll 1$, for which $r_p/\dot{r}_p = -t\nu/B$, hence we deduce $\Delta T/\dot{M}l_p = -0.5$ (see, for example Syer & Clarke 1995; Ivanov et al. 1999);

(iii) migration at high K where $\Delta T/\dot{M}l_p \sim 0.5$ from our numerical results.

We can combine the two limits (a) and (b) as $\Delta T/|\dot{M}l_p| = -0.5/(B+1)$; then we put all of these considerations together to obtain

$$\frac{r_p}{\dot{r}_p} = \begin{cases} -\frac{B+1}{B}\cdot t_\nu & \text{if } K < K_{\rm lim} \\ \frac{1}{B}\cdot t_\nu & \text{if } K > K_{\rm lim} \end{cases} \tag{20}$$

where $K_{\rm lim}$ is the limiting value which determines the transition from inward to outward migration. For the purpose of the toy model, we take $K_{\rm lim} = 1.5\cdot 10^4$ (as estimated from Fig. 7).

Given all these considerations, we can define a function $g(K)$ such that[9]

$$\frac{r_p}{\dot{r}_p} = \frac{1}{g(K)}\frac{B+1}{B}t_\nu. \tag{21}$$

We therefore need a function with the following properties: for high K and low B, $g(K) \sim 1$, to obtain the lower case in equation (20); for low K, we want $g(K) \sim -1$, to recover the classical prediction for Type II migration (upper case in equation 20). Note that in deriving the formula in equation (21) we have not considered the case with high K and high B, because for the typical disc parameters and plausible planet location, it is unlikely to obtain this combination; consequently, for high values of B we expect the planet to migrate inward following the 'classical' Type II migration rate (as analysed in Scardoni et al. 2020). We thus model the functional form of $g(K)$ as

$$g(K) = \tanh\left(\frac{K - K_{\rm lim}}{W}\right), \tag{22}$$

where W controls the width of the transition in K over which $g(K)$ changes sign. We then estimate the planet migration by solving the following equation:

$$\dot{r}_p = r_p g(K)\frac{B}{B+1}\frac{1}{t_\nu}, \tag{23}$$

where we underline that all the quantities on the right hand side are functions of r_p (and hence time).

Since planets are expected to migrate inward (outward) for K values smaller (bigger) than $K_{\rm lim} = 1.5\times 10^4$, and because K increases during inward migration and decreases during outward migration in the case of flaring discs ($f > 0$ in equation 24 below), we expect them to always migrate towards the location of the disc where $K = K_{\rm lim}$. We then call $r_{\rm lim}$ the radius corresponding to $K_{\rm lim} = 1.5\times 10^4$ that is therefore an 'attractor' for migrating planets

$$r_{\rm lim} = \left(\frac{q^2}{K_{\rm lim}\alpha_0 h_0^5}\right)^{1/(a+5f)}, \tag{24}$$

where $\alpha = \alpha_0 r^a$ and $h = h_0 r^f$.

Note that in the toy model we do not include the effect of eccentricity growth, because we develop the toy model in the case of Jovian mass planets where eccentricity growth is very modest. We neither include the effect of the planet on the surface density profile, because by comparing the evolution of the disc with and without a Jupiter mass planet we found that the two systems behave similarly over the long time-scales.

[6] As underlined in Section 3.2.1, $\Delta T/\dot{M}l_p$ does not depend on the disc mass only when the planetary orbit maintains a low eccentricity; this is best satisfied for the $1m_J$ case, which we therefore use in the toy model.

[7] Here we use r_p instead of a_p because we are assuming circular orbits.

[8] We define $t_\nu = 4r^2/3\nu$.

[9] Note that we define $g(K)$ in this way because we want it to be proportional to $\Delta T/|\dot{M}l_p|$, which is the quantity that we have analysed in the previous sections.

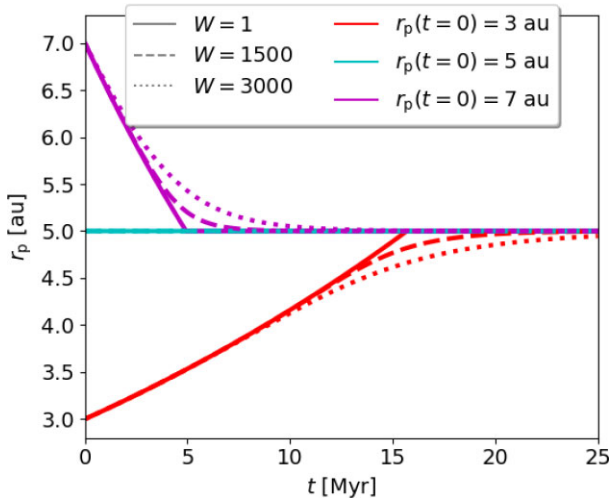

Figure 11. Toy model for a planet of mass $m_p = 1\, m_j$ and a disc characterized by $\alpha = 0.001$, $h = 0.02$ at 1 au and flaring index 0.25, producing a stalling radius located at 5 au. The different colours show the planet migration tracks for an initial planet location equal to 3 au (red lines), 5 au (cyan lines), and 7 au (magenta lines). The different line styles refer to different choices of parameter W: $W = 1$ for the solid line; $W = 1500$ for the dashed line; $W = 3000$ for the dotted line. At 5 au, the disc to planet mass ratio is $B = 0.1$, while the viscous time-scale is $t_\nu(5\text{au}) = 1.6$ Myr.

5.1 Toy model in a non-evolving disc

We first define a disc model characterized by $\alpha = 0.001$ (constant throughout the disc), thus $\nu \propto r^{2f+1/2}$; and $\Sigma(r) = \Sigma(r_1)(r/r_1)^{-1}$, where r_1 is the value of 1 au in code units, and $\Sigma(r_1)$ is chosen to have $B_{5\text{au}} = 0.1$ at 5 au,[10] corresponding to $M_{\text{disc}} \sim 0.001\ \text{M}_\odot$ for a disc of 100 au. As the planet migrates (in either direction), the value of B varies as[11]

$$B(t) = B_{5\text{au}} \cdot \left(\frac{r_p(t)}{5\text{ au}}\right). \tag{25}$$

To design a disc model with $r_{\text{lim}} = 5$ au (i.e. the location of Jupiter), the disc aspect ratio at 1 au is taken equal to 0.02, while the flaring index is 0.25.

We then insert a Jupiter mass planet and solve equation (23). In Fig. 11, we illustrate the behaviour of r_{lim} as an attractor, considering three different models: a planet initially located at $r_p(t=0) = 3\text{ au} < r_{\text{lim}}$, which then migrates outwards until stalling at 5 au (red lines); for $r_p(t=0) = 5\text{ au} = r_{\text{lim}}$ the planet stalls at its initial location (cyan line); for $r_p(t=0) = 7\text{ au} > r_{\text{lim}}$, instead, the planet migrate inwards (magenta lines). The solid, dashed, and dotted lines refer to values of parameter W in equation (22) equal to 1, 1500, and 3000, respectively.

For the inward migrating planet (initially at 7 au), the time-scale required to reach the stalling radius in all cases is less than 10 Myr, which means that the planet can reach the stalling location during the disc lifetime. In the case of the planet initially located at 3 au, instead, the planet migrates to 4 au in 10 Myr, but requires ~ 15 Myr to reach the stalling radius. We caution, however, that the time-scale on which the planet makes its final approach to the stalling radius is very sensitive to the choice of W in the function $g(K)$; this underlines the importance of further simulations to explore the form of $g(K)$. We furthermore notice that as the obtained migration time-scale is comparable to the disc lifetime, we would expect the disc density to evolve in time over the planet's migration and model this possibility in the following section.

5.2 Toy model in an evolving disc

Since the planet migration time-scale expected from the toy model is comparable to the disc lifetime, we define a variant of the toy model to take into account of the density evolution during migration.

For this purpose, while solving equation (23) we evolve the density profile at each time-step according to the self-similar solution by Lynden-Bell & Pringle (1974)

$$\Sigma(R,t) = \frac{M_{\text{disc},0}}{2\pi R_{s,0}}(2-b)\left(\frac{R}{R_{s,0}}\right)^{-b} \tau^{-\eta} \times \exp\left[-\frac{(R/R_{s,0})^{2-b}}{\tau}\right], \tag{26}$$

where $M_{\text{disc},0}$ is the initial disc mass, defined by the choice of the density profile and the initial disc scale radius; $R_{s,0}$ is the initial scale radius; b is a parameter of the model that is the power-law exponent for the radial variation of the viscosity that we fix to 1 for consistency with the previous section; $\eta = (5/2-b)/(2-b)$; τ is defined as $\tau = 1 + t/t_\nu$, with $t_\nu = R_s^2/[3(2-b)^2\nu(R_s)]$. The surface density will thus evolve on the viscous time-scale of the instantaneous scale radius

$$R_s(t) = R_{s,0}\left[\frac{\tau}{2(2-b)}\right]^{\frac{1}{2-b}}. \tag{27}$$

We show in Fig. 12 the evolution tracks for a Jupiter mass planet initially located at 3 au (left-hand panel) and 7 au (right-hand panel), in a disc whose density is evolving as described above. In both cases, we consider different models, characterized by a range of initial scale radii (50 au with the solid lines, 100 au with the dashed lines, and 200 au with the dotted lines), and a range of B_0 (from 0.09 to 0.5, see the plot legend). For reference, the initial viscous time-scale at the planet location are $t_\nu(3\text{ au}) \sim 1$ Myr, and $t_\nu(7\text{ au}) \sim 2.5$ Myr; while the viscous time-scales at the chosen scale-radii are $t_\nu(50\text{ au}) = 4.4$ Myr, $t_\nu(100\text{ au}) = 8.9$ Myr, $t_\nu(200\text{ au}) = 17.7$ Myr. Since the density is reduced while the disc evolves, the migration time-scale becomes longer in both the cases when we consider an evolving disc (compare the red lines to Fig. 11). In fact, a decrease in the surface density causes the instantaneous value of the parameter B to decrease, making the migration time-scale longer. This means that models characterized by faster density evolution (i.e. those with lower $R_{s,0}$) slow down the migration more effectively than those characterized by slower density evolution; this behaviour can be easily seen in Fig. 12 by comparing the dotted, dashed, and solid lines with the same colour (i.e. with different $R_{s,0}$ but same $B_{5\text{au}}$).

Even more important is the effect of considering different $B_{5\text{au}}$ values, with the migration time-scale increasing while $B_{5\text{au}}$ decreases. Furthermore we notice that in all the models the planet starting from 3 au is more affected by the surface density time evolution, because the value of B at its initial location is lower, thus it is more sensitive to further reductions in the local density value. In contrast, the planet starting from 7 au reaches the stalling radius before decreasing significantly the value of B, so that it can reach the stalling radius in $\lesssim 10$ Myr even in the model characterized by the lowest $B_{5\text{au}}$ and the smallest $R_{s,0}$ (see the red solid line in the right-hand panel).

This result has interesting implication for the properties of a system characterized by outward migrating planets. From Fig. 12, we can

[10] In the rest of the paper we will refer to the value of B at 5 au as $B_{5\text{au}}$; while we will indicate as B the value at the planet location.

[11] Note that the dependence of B on r_p depends on the chosen density profile: if $\Sigma \propto r^{-s}$, then $B \propto r_p^{2-s}$.

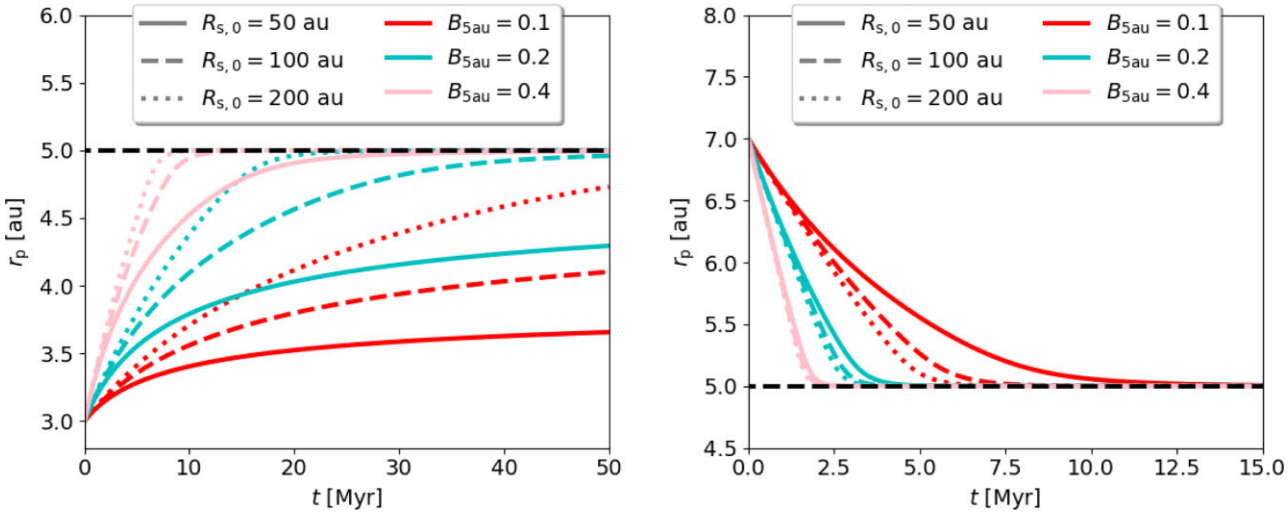

Figure 12. Toy model for a Jupiter mass planet initially located at 3 au (left-hand panel) and 7 au (right-hand panel), and migrating in a disc evolving according to the Lynden-Bell & Pringle (1974) self-similar solution. The different colours and line styles refer to disc models characterized by a range of initial scale radii and B_{5au}, whose values are indicated in the legend.

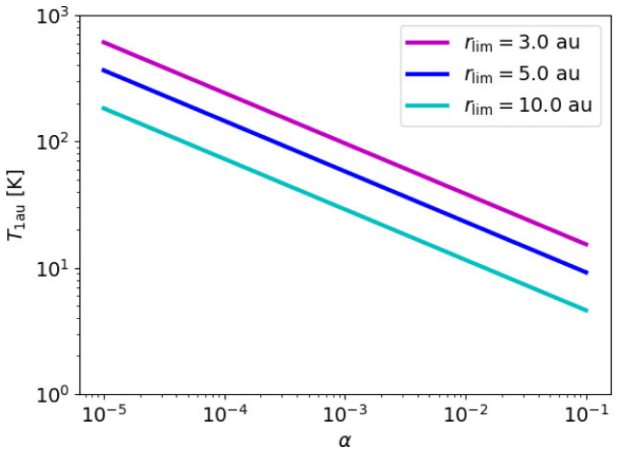

Figure 13. Disc temperature at 1 au as a function of the viscosity parameter α, required to have a Jupiter mass planet stalling at r_0; the magenta line correspond to $r_0 = 3$ au, the blue line correspond to $r_0 = 5$ au, the cyan line correspond to $r_0 = 10$ au.

deduce that to have a Jupiter mass planet migrating to 5 au in our model, we need to take either $B_{5au} \gtrsim 0.4$, or we can decrease it to $B_{5au} \gtrsim 0.2$ if we take a disc with $R_{s,0} \gtrsim 100$ au. For lower B_{5au} values, even in the case of discs with large scale radii, the planet fails to migrate to the stalling radius in $\lesssim 10$ Myr; none the less, we still expect some outward migration for those planets, with a final radius which is determined by the disc lifetime rather than by the value of the stalling radius.

5.3 Stalling radius and disc properties

In this section, we focus on how the disc properties affect the location of the stalling radius. To investigate this problem, we consider a Jupiter mass planet, and we compute the disc's properties required to have the planet stalling at a given radius r_0. In the left-hand panel of Fig. 13, we consider three different stalling radii – 3 au (magenta line), 5 au (blue line), 10 au (cyan line) – and for each we plot the disc temperature T at 1 au as a function of the α parameter. Focusing first on the blue line, we notice that for a Jupiter mass planet that stalls 5 au the disc temperature at 1 au may vary from $T \gtrsim 10$ K to $T \gtrsim 10^2$ K, when we choose values for the α parameter in the range $\alpha \sim 10^{-4}$ to 10^{-2}.[12] Since $T \gtrsim 10$ to 10^2 K at 1 au is a sensible temperature range for protoplanetary discs, this model is in agreement with the findings by Fernandes et al. (2019) and Nielsen et al. (2019) who suggest that around solar-like stars there is a peak in the number of giant planets located at ∼5 au from the star. We further notice that for higher disc temperature the planet stalling radius decreases for fixed α because for a hotter disc, a larger region of the disc is in the low K (shallow gap) regime where inward migration is expected.

If we consider more massive stars, the planet to star mass ratio decreases as $q \propto M_*^{-1}$, whereas the disc aspect ratio $h_0 \propto \sqrt{T/M_*}$, with $T \propto M_*^{\xi}$ (the relation is sub-linear, and the exact value of ξ depends on the assumed stellar mass-luminosity relation). Using these scale relations in equation (24), we find

$$r_{lim} \propto M_*^{\frac{1-5\xi}{2(a+5f)}}, \tag{28}$$

therefore we expect the stalling radius value to increase (decrease) with increasing stellar mass for $\xi < 1/5$ ($\xi > 1/5$). At fixed radius, the temperature approximately scales as $T \propto M_*^{0.15}$ (Sinclair et al. 2020), we therefore expect that for the typical disc the location of the stalling radius increases for higher stellar mass; this is in agreement with the results from Nielsen et al. (2019) that higher mass stars should have the peak of the Jupiter mass planet distribution at higher radius with respect to solar mass stars.

6 IMPLICATIONS

Planetary population synthesis models for giant planets are widely based on the theory of Type II migration (Ida & Lin 2004, 2008; Mordasini, Alibert & Benz 2009a; Mordasini et al. 2009b; Ida et al.

[12]Note that in our model we consider a constant α value, for which it is common to consider $\alpha \sim 10^{-4}$ to 10^{-3}; if we consider instead the fact that α depends on the specific location in the disc, direct turbulence measurements (e.g. Carr, Tokunaga & Najita 2004) suggest that at sub-au radii $\alpha \sim 10^{-2}$ is more typical.

2018; Bitsch et al. 2019). In its classic form this involves inward migration on a viscous time-scale which decelerates at the point that the planet mass becomes comparable with the local disc mass. However, since the viscous time-scale decreases with decreasing orbital radius, the net effect is that the planet arrives at the disc inner edge in a finite time (Syer & Clarke 1995; Ivanov et al. 1999). The continued inward driving by the disc is related to the assumption of zero flow past the planet so that material can always accumulate exterior to the planetary orbit and drive continued inward migration.

This paper has demonstrated that even in calculations where the planetary orbital elements are allowed to evolve, giant planets do *not* arrive at the disc inner edge in a finite time. This is because as the planet migrates in to regions of the disc where the local disc mass dominates the planet mass, the disc establishes a quasi-steady state flow past the planet (cf Dempsey et al. 2020, 2021), preventing the inexorable extraction of angular momentum of the planet by material accumulating outside the planetary orbit. Moreover, as previously analysed by Dempsey et al. (2020, 2021) the sign of the torque depends on the quasi-steady state structure of the gas in the vicinity of the planet. A key point is that the disc interior to the planet is always in a steady state and so, in order to ensure net zero accumulation of angular momentum in this region, must impart a spin-up torque to the planet of magnitude $\dot{M}l_{\rm p}$. On the other hand, the disc outside the planet is never globally in a steady state and thus the angular momentum that it extracts from the planet is not constrained to be $\dot{M}l_{\rm p}$, its magnitude depending on the structure of the gap exterior to the planet. Thus for wider gaps (due to either higher planet mass or lower disc aspect ratio h), the spin-down torque on the planet is reduced as a result of the substantial clearing external to the planetary orbit: Fig. 5 demonstrates that the asymmetry between surface density interior and exterior to the planet becomes more pronounced for higher planet masses and colder (geometrically thinner) discs. We show that even in cases where the planet acquires a significant eccentricity as a result of interaction in the disc (i.e. those cases where the inner edge of the gap extends to close to the 3:1 mean motion resonance), the evolution of the planetary semimajor axis is well described in terms of a simple switch at a value of K (equation 22) of around 1.5×10^4 (Fig. 7).

We illustrate in Section 5 the implementation of some toy models that incorporate this evolutionary phenomenology. We examined the possibility that the location of zero torque might be imprinted on the architecture of planetary systems. As expected, the planetary evolutionary tracks demonstrate a convergence towards this attractor (Fig. 11), located at 5 au given the planet mass and normalization of the disc temperature profile (see Fig. 13 for the sensitivity of the attractor location to disc parameters for a Jovian mass planet). However, the evolution may be too slow for planets to necessarily get close to the attractor location. First of all, the attainment of high K values (associated with planet stalling) is favoured by relatively low alpha values where the viscous time-scale is relatively long. Secondly, the speed of convergence upon the attractor location depends on the range of disc radii over which the torque magnitude undergoes a sign switch. Clearly, if this occurs relatively gradually, there will be a broad radial range where the torque values are low and therefore the evolution towards the attractor becomes very slow. Our present simulation set (right hand panel of Fig. 7) does not allow us to tightly constrain the behaviour near the point of zero torque. Finally, because the planet is not damming up the disc upstream of the planetary orbit, the disc's effect on the planet is progressively weakening on a time-scale set by the viscous time-scale of the outer disc. Thus whether the planet can be driven to the attractor depends on the migration time-scale (t_{ν_0}/B) compared with the viscous time-scale of the outer disc: as illustrated in Fig. 12, efficient driving of the planet to its attractor location during the observed lifetime of protoplanetary discs (e.g. Alcalá et al. 2014; Manara et al. 2016) is achieved for relatively high B values (corresponding to fast migration time-scale), and high $R_{\rm s,0}$ values (corresponding to slow viscous evolution). Given these considerations, which depend on poorly constrained parameters such as the value of α and the form of the torque's dependence on gap shape in the region close to the location of zero net torque, it would be premature to argue that this process should impose a strong signature by piling up planets at a specific orbital location. Nevertheless, it is expected that Jovian mass planets should accumulate in the 1–10 au range by this process.

What is certainly clear, however, is that these results preclude the production of hot Jupiters by disc mediated migration, at least in a non-self-gravitating disc.[13] This is because it is implausible that the disc gas surface density in the inner disc would ever be high enough to maintain $B > 1$ (where roughly viscous time-scale inward migration is expected) right down to the inner edge of the disc. For example, for a Jupiter mass planet at 0.1 au, $B = 1$ corresponds to such a high surface density that the total disc mass would likely exceed a solar mass within a few au. If the candidate hot Jupiter in the Classical T Tauri star CI Tau (Johns-Krull et al. 2016) is confirmed (see counterarguments by Donati et al. 2020) it would then present a puzzle concerning how such a massive planet would have arrived in the innermost disc by an age of a few Myr. Rapid inward migration of giant planets during the earliest self-gravitating disc phase has been proposed by Baruteau, Meru & Paardekooper (2011) and Malik et al. (2015), though more recent works suggest that even then it may not be possible to migrate into the innermost disc (Stamatellos & Inutsuka 2018; Rowther & Meru 2020).

It is also interesting to notice that the existence of planet traps have already been suggested in a series of papers by Hasegawa & Pudritz (2013, 2014), for lower mass planets (or planetary cores). They showed that low mass planets can be trapped at zero torque locations, potentially produced at disc radii characterized by significant density/thermal gradients, such as dead zone boundaries and ice lines.

We finally caution that this work relies on the assumption that only one planet is formed in the disc. In the case that multiple planets are formed, simulations including more migrating planets are needed.

7 CONCLUSIONS

In this work, we have presented a suite of long term (300–600k planet orbits), 2D hydrodynamical simulations to test and expand recent findings by Dempsey et al. (2020, 2021) of an empirical correlation between the direction of planet migration and the value of the modified gap-opening parameter K'. We extend the torque analysis to systems with finite disc mass by considering a live planet allowed to modify its orbital parameters.

Our live planet simulations confirm that there is a switch between inward and outward migration that is associated with the creation of deep gaps in the disc. Gap depth is an increasing function of planet mass and a decreasing function of disc aspect ratio and can alternatively be parametrized by the quantities $K' = q^2/(\alpha h^3)$ (equation 6) and $K = q^2/(\alpha h^5)$ (equation 12). Our simulations suggest

[13]Note that the contrary conclusion by Rosotti et al. (2017) was a result of these authors not adopting viscous boundary conditions so that the loss of the inner disc led to a net negative torque on the planet: the Rosotti et al. (2017) simulation corresponds to the diamond for the L-m13-h036 simulation in Fig. 9.

that K may be the better ordering parameter for describing planetary migration (see right-hand panel of Fig. 6) and that the switch from inward to outward migration occurs at $K_{\rm lim} = 1.5 \times 10^4$.

We further notice that, regardless the choice of the ordering parameter, as the planet mass increases some dependence on B_0 of the torques acting on the planet is revealed; this effect could not be seen in fixed planet simulations, where the normalized torque $\Delta T/|\dot{M}l_{\rm p}|$ values are disc mass independent by construction. This means that if we consider low mass planets, the fixed-planet simulations by Dempsey et al. (2020, 2021) are a good approximation of the planets' migration; if we consider higher mass planets, the results are modified by the growth of the planet's eccentricity in a way that depends on the disc mass (Ragusa et al. 2018; Teyssandier & Lai 2019). Nonetheless we showed that, by disentangling the contribution to the torque due to the semimajor axis variation from the contribution due to the eccentricity evolution, the massive planet migration is well described by the change of sign of the disentangled torque at $K_{\rm lim} \sim 1.5 \times 10^4$. It is a general feature of protoplanetary discs with realistic heating that the aspect ratio of the disc increases with radius and thus that K is a decreasing function of radius. We thus predict inward (outward) migration for radii exterior (interior) to the location where K has its limiting value.

We then model the migration behaviour of massive planets by describing the dependence of migration on the parameter K. We evaluate this migration in the context of the secular evolution of a viscous disc. This model allows us to obtain the following results:

(i) Since planets migrate inwards (outwards) for $K < K_{\rm lim}$ ($K > K_{\rm lim}$), they tend to go towards the location in the disc where $K = K_{\rm lim}$. We thus propose the existence of a 'stalling radius' defined by the location where $K = K_{\rm lim}$ (i.e. the location of zero torque on the planet).

(ii) We study the dependence of the stalling radius on the disc parameters (temperature and α viscosity parameter), finding that typical disc parameters enable stalling radii in the range 3–10 au, in agreement with the peak in the Jupiter distribution at a few au (Fernandes et al. 2019; Nielsen et al. 2019).

(iii) When we include the effect of disc density evolution in the model, the migration is slowed down, due to the density reduction with time (which reduces the parameter B). As a consequence, the planet migration towards the stalling radius might be limited by the disc lifetime in rapidly evolving systems characterized by relatively low B_0.

The toy model suggests that while planets should migrate towards a stalling radius set by the planet mass and disc aspect ratio, whether or not they attain their stalling radii depends both on the initial location of the planet and the overall radial extent of the disc, since the latter determines the rate at which the disc surface density declines. Thus it is likely that this effect does not imprint a strong pile up of planets at their respective stalling radii but rather causes them to occupy a broad-band of radii in the range 3−10 au. Future quantification of the torque dependence on K in the vicinity of $K_{\rm lim}$ will help to constrain this further. In any case we do not expect planets to be able to move in from this band by disc mediated migration, thus posing a difficulty for hot Jupiter formation at early times.

ACKNOWLEDGEMENTS

We would like to thank the referee for the careful reading of this paper and for the useful comments. CES thanks Peterhouse Cambridge for a Ph.D. studentship. RAB acknowledges the Royal Society University Research Fellowship. GR acknowledges support from the Netherlands Organisation for Scientific Research (NWO, programme number 016.Veni.192.233) and from an STFC Ernest Rutherford Fellowship (grant number ST/T003855/1). RDA and ER gratefully acknowledge funding from the European Research Council (ERC) under the European Union's Horizon 2020 research and innovation programme (grant agreement no. 681601); RDA also acknowledges funding from STFC Consolidated grant ST/W000857/1. ER acknowledges funding from the European Research Council (ERC) under the European Union's Horizon 2020 research and innovation programme (grant agreement no. 864965). This work has also been supported by the European Union's Horizon 2020 research and innovation programme under the Marie Sklodowska-Curie grant agreement number 823823 (DUSTBUSTERS). This work was in part performed using the Cambridge Service for Data Driven Discovery (CSD3), part of which is operated by the University of Cambridge Research Computing on behalf of the STFC DiRAC HPC Facility (www.dirac.ac.uk). The DiRAC component of CSD3 was funded by BEIS capital funding via STFC capital grants ST/P002307/1 and ST/R002452/1, and STFC operations grant ST/R00689X/1. This work was in part performed using the DiRAC Data Intensive service at Leicester, operated by the University of Leicester IT Services, which forms part of the STFC DiRAC HPC Facility (www.dirac.ac.uk). The equipment was funded by BEIS capital funding via STFC capital grants ST/K000373/1 and ST/R002363/1, and STFC DiRAC Operations grant ST/R001014/1. DiRAC is part of the National e-Infrastructure.

DATA AVAILABILITY

The code used to perform the simulations contained in this paper (FARGO3D; Benítez-Llambay & Masset 2016) is available at http://fargo.in2p3.fr.

REFERENCES

Alcalá J. M. et al., 2014, A&A, 561, A2
Artymowicz P., 1993, ApJ, 419, 166
Baruteau C., Meru F., Paardekooper S. J., 2011, MNRAS, 416, 1971
Baruteau C. et al., 2014, in Beuther H., Klessen R. S., Dullemond C. P., Henning T., eds, Protostars and Planets VI. Univ. Arizona Press, p. 667
Benítez-Llambay P., Masset F. S., 2016, ApJS, 223, 11
Bitsch B., Crida A., Morbidelli A., Kley W., Dobbs-Dixon I., 2013, A&A, 549, A124
Bitsch B., Izidoro A., Johansen A., Raymond S. N., Morbidelli A., Lambrechts M., Jacobson S. A., 2019, A&A, 623, A88
Carr J. S., Tokunaga A. T., Najita J., 2004, ApJ, 603, 213
Crida A., Morbidelli A., 2007, MNRAS, 377, 1324
Crida A., Morbidelli A., Masset F., 2006, Icarus, 181, 587
D'Angelo G., Bate M. R., Lubow S. H., 2005, MNRAS, 358, 316
de Val-Borro M. et al., 2006, MNRAS, 370, 529
Dempsey A. M., Lee W.-K., Lithwick Y., 2020, ApJ, 891, 108
Dempsey A. M., Muñoz D. J., Lithwick Y., 2021, ApJL, 918, L36
Donati J. F. et al., 2020, MNRAS, 491, 5660
Duffell P. C., Chiang E., 2015, ApJ, 812, 94
Duffell P. C., Haiman Z., MacFadyen A. I., D'Orazio D. J., Farris B. D., 2014, ApJ, 792, L10
Dürmann C., Kley W., 2015, A&A, 574, A52
Fernandes R. B., Mulders G. D., Pascucci I., Mordasini C., Emsenhuber A., 2019, ApJ, 874, 81
Fung J., Chiang E., 2016, ApJ, 832, 105
Fung J., Shi J.-M., Chiang E., 2014, ApJ, 782, 88
Goldreich P., Sari R., 2003, ApJ, 585, 1024
Goldreich P., Tremaine S., 1979, ApJ, 233, 857
Goldreich P., Tremaine S., 1980, ApJ, 241, 425

Hallam P. D., Paardekooper S. J., 2018, MNRAS, 481, 1667
Hasegawa Y., Pudritz R. E., 2013, ApJ, 778, 78
Hasegawa Y., Pudritz R. E., 2014, ApJ, 794, 25
Ida S., Lin D. N. C., 2004, ApJ, 604, 388
Ida S., Lin D. N. C., 2008, ApJ, 673, 487
Ida S., Tanaka H., Johansen A., Kanagawa K. D., Tanigawa T., 2018, ApJ, 864, 77
Ivanov P. B., Papaloizou J. C. B., Polnarev A. G., 1999, MNRAS, 307, 79
Johns-Krull C. M. et al., 2016, ApJ, 826, 206
Kanagawa K. D., Tanaka H., Muto T., Tanigawa T., Takeuchi T., 2015, MNRAS, 448, 994
Kanagawa K. D., Muto T., Tanaka H., Tanigawa T., Takeuchi T., Tsukagoshi T., Momose M., 2016, PASJ, 68, 43
Kanagawa K. D., Tanaka H., Szuszkiewicz E., 2018, ApJ, 861, 140
Kley W., Dirksen G., 2006, A&A, 447, 369
Kley W., Nelson R. P., 2012, ARA&A, 50, 211
Lega E. et al., 2021, A&A, 646, A166
Lin D. N. C., Papaloizou J., 1979, MNRAS, 186, 799
Lin D. N. C., Papaloizou J. C. B., Kley W., 1993, ApJ, 416, 689
Lubow S. H., D'Angelo G., 2006, ApJ, 641, 526
Lynden-Bell D., Pringle J. E., 1974, MNRAS, 168, 603
Malik M., Meru F., Mayer L., Meyer M., 2015, ApJ, 802, 56
Manara C. F. et al., 2016, A&A, 591, L3
Mayor M., Queloz D., 1995, Nature, 378, 355
Mordasini C., Alibert Y., Benz W., 2009a, A&A, 501, 1139
Mordasini C., Alibert Y., Benz W., Naef D., 2009b, A&A, 501, 1161
Nielsen E. L. et al., 2019, AJ, 158, 13
Paardekooper S.-J., Dong R., Duffell P., Fung J., Masset F. S., Ogilvie G., Tanaka H., 2022, preprint (arXiv:2203.09595)
Papaloizou J. C. B., 2021, ExoFrontiers. IOP Publishing, p. 13–1
Papaloizou J. C. B., Terquem C., 2006, Rep. Prog. Phys., 69, 119
Ragusa E., Rosotti G., Teyssandier J., Booth R., Clarke C. J., Lodato G., 2018, MNRAS, 474, 4460
Robert C. M. T., Crida A., Lega E., Méheut H., Morbidelli A., 2018, A&A, 617, A98
Rosotti G. P., Booth R. A., Clarke C. J., Teyssandier J., Facchini S., Mustill A. J., 2017, MNRAS, 464, L114
Rowther S., Meru F., 2020, MNRAS, 496, 1598
Scardoni C. E., Rosotti G. P., Lodato G., Clarke C. J., 2020, MNRAS, 492, 1318
Shakura N. I., Sunyaev R. A., 1973, A&A, 24, 337
Sinclair C. A., Rosotti G. P., Juhasz A., Clarke C. J., 2020, MNRAS, 493, 3535
Stamatellos D., Inutsuka S.-i., 2018, MNRAS, 477, 3110
Syer D., Clarke C. J., 1995, MNRAS, 277, 758
Teyssandier J., Lai D., 2019, MNRAS, 490, 4353
Teyssandier J., Ogilvie G. I., 2016, MNRAS, 458, 3221
Teyssandier J., Ogilvie G. I., 2017, MNRAS, 467, 4577
Thun D., Kley W., Picogna G., 2017, A&A, 604, A102
Veras D., Armitage P. J., 2004, MNRAS, 347, 613
Ward W. R., 1998, in Woodward C. E., Shull J. M., Thronson Harley A. J., eds, ASP Conf. Ser. Vol. 148, Origins. Astron. Soc. Pac., San Francisco, p. 338

APPENDIX A: TEST INNER BOUNDARY EFFECTS

From Fig. 2, we noticed that in simulation L-m13-h036 (i.e. the light disc case with 13 m_j planet and $h = 0.036$), the planet grows significantly its eccentricity so that its pericentre distance is only ∼2.5 times the inner disc edge. Since at the inner boundary, we are applying wave killing boundary conditions (see Section 2), we must ensure that at the in simulation L-m13-h036 the planet evolution is not affected by numerical effects due to its closeness to the inner boundary when it is at the pericentre. We thus present here the results from a simulation test, characterized by all the same characteristics as those of simulation L-m13-h036, apart from the inner radius and the damping region, which are both taken to be half of their original values: we take $r_{in} = 0.1$, the damping is taken from r_{in} to $r = 0.15$; we also increase the number of radial cells in order to obtain the same radial resolution as the original simulation run.

In Fig. A1, we show the semimajor axis (left-hand panel) and eccentricity (right-hand panel) as a function of orbit, for both the original L-m13-h036 run (magenta line) and the simulation test with $r_{in} = 0.1$ (black dashed line). We notice that the semimajor and eccentricity evolution is essentially the same in both the runs, confirming that the planet evolution in simulation L-m13-h036 is not affected by boundary numerical effects.

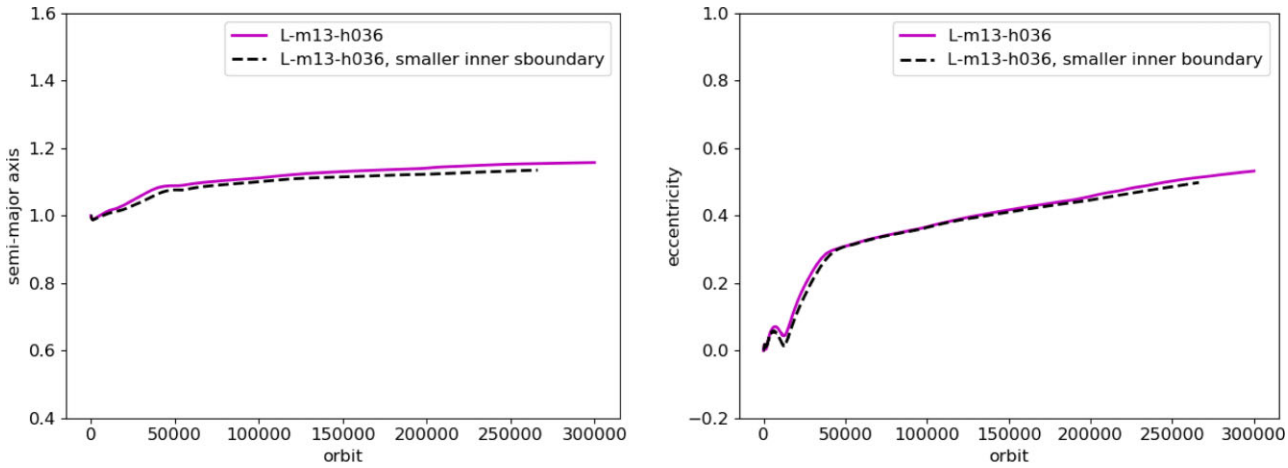

Figure A1. Semimajor axis (left-hand panel) and eccentricity (right-hand panel) evolution in the light disc case with 13 m_j planet and $h = 0.036$. The magenta line shows the planet evolution in the original simulation run L-m13-h = 0.026, with $r_{in} = 0.2$; the black dashed line shows the result from the simulation test, characterized by $r_{in} = 0.1$.

This paper has been typeset from a TEX/LATEX file prepared by the author.